


















RESEARCH ARTICLE | JULY 06 2022

Broadband stimulated Raman imaging based on multi-channel lock-in detection for spectral histopathology

Alejandro De la Cadena ✉; Federico Vernuccio ; Andrea Ragni ; Giuseppe Sciortino ; Renzo Vanna ; Carino Ferrante ; Natalia Pediconi ; Carlo Valensise ; Luca Genchi ; Sergey P. Laptinok ; Andrea Doni ; Marco Erreni ; Tullio Scopigno ; Carlo Liberale ; Giorgio Ferrari ; Marco Sampietro ; Giulio Cerullo ; Dario Polli ✉



APL Photonics 7, 076104 (2022)
<https://doi.org/10.1063/5.0093946>



Articles You May Be Interested In

Automatic mitosis detection in histopathology images & grading using SVM classifier

AIP Conference Proceedings (December 2021)

Comparative analysis of image denoising techniques for histopathology images

AIP Conf. Proc. (November 2023)

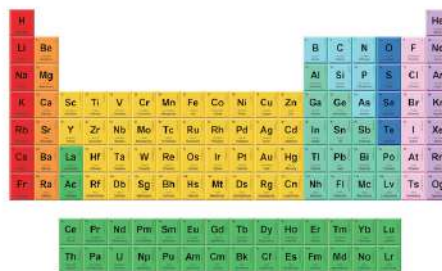
Transfer learning VGG for histopathological lung cancer image classification

AIP Conf. Proc. (July 2024)



THE MATERIALS SCIENCE MANUFACTURER®

Now Invent.™



American Elements
 Opens a World of Possibilities

...Now Invent!

www.americanelements.com

Broadband stimulated Raman imaging based on multi-channel lock-in detection for spectral histopathology

Cite as: APL Photon. 7, 076104 (2022); doi: 10.1063/5.0093946

Submitted: 31 March 2022 • Accepted: 8 June 2022 •

Published Online: 6 July 2022



Alejandro De la Cadena,^{1,a)} Federico Vernuccio,¹ Andrea Ragni,² Giuseppe Sciortino,²
Renzo Vanna,³ Carino Ferrante,^{4,5,6,7} Natalia Pediconi,⁴ Carlo Valensise,⁸ Luca Genchi,⁹
Sergey P. Laptanok,⁹ Andrea Doni,¹⁰ Marco Erreni,¹⁰ Tullio Scopigno,^{4,5,7} Carlo Liberale,¹¹
Giorgio Ferrari,² Marco Sampietro,² Giulio Cerullo,^{1,3} and Dario Polli^{1,3,a)}

AFFILIATIONS

¹Physics Department, Politecnico di Milano, Milan, Italy

²Electronics, Information, and Bioengineering Department, Politecnico di Milano, Italy

³Institute for Photonics and Nanotechnologies, CNR (IFN-CNR), Milan, Italy

⁴Physics Department, Università di Roma "La Sapienza," Roma, Italy

⁵Italian Institute of Technology, Center for Life Nano-and Neuro-Science, Roma, Italy

⁶ENEA, FSN-FISS-SNI Laboratory, Roma, Italy

⁷Italian Institute of Technology, Graphene Labs, Genoa, Italy

⁸Enrico Fermi Research Center, Roma, Italy

⁹Biological and Environmental Science and Engineering Division, King Abdullah University of Science and Technology (KAUST), 23955 Thuwal, Saudi Arabia

¹⁰Unit of Advanced Optical Microscopy, IRCCS Humanitas Research Hospital, Milan, Italy

¹¹Computer, Electrical and Mathematical Sciences Division, King Abdullah University of Science and Technology (KAUST), 23955 Thuwal, Saudi Arabia

^{a)}Authors to whom correspondence should be addressed: alejandrodelaacadena@polimi.it and dario.polli@polimi.it

ABSTRACT

Spontaneous Raman microscopy reveals the chemical composition of a sample in a label-free and non-invasive fashion by directly measuring the vibrational spectra of molecules. However, its extremely low cross section prevents its application to fast imaging. Stimulated Raman scattering (SRS) amplifies the signal by several orders of magnitude thanks to the coherent nature of the nonlinear process, thus unlocking high-speed microscopy applications that provide analytical information to elucidate biochemical mechanisms with subcellular resolution. Nevertheless, in its standard implementation, narrowband SRS provides images at only one frequency at a time, which is not sufficient to distinguish constituents with overlapping Raman bands. Here, we report a broadband SRS microscope equipped with a home-built multichannel lock-in amplifier simultaneously measuring the SRS signal at 32 frequencies with integration time down to 44 μ s, allowing for detailed, high spatial resolution mapping of spectrally congested samples. We demonstrate the capability of our microscope to differentiate the chemical constituents of heterogeneous samples by measuring the relative concentrations of different fatty acids in cultured hepatocytes at the single lipid droplet level and by differentiating tumor from peritumoral tissue in a preclinical mouse model of fibrosarcoma.

© 2022 Author(s). All article content, except where otherwise noted, is licensed under a Creative Commons Attribution (CC BY) license (<http://creativecommons.org/licenses/by/4.0/>). <https://doi.org/10.1063/5.0093946>

INTRODUCTION

Raman microscopy is a powerful technique to image biological specimens, such as cells and tissues, in a label-free and non-invasive manner. It measures the vibrational spectrum of the molecules^{1,2} contained in a diffraction-limited focal spot, providing direct information on the chemical composition and structure of the sample. Spontaneous Raman (SR) imaging uses the whole information encoded within the vibrational spectrum as a source of contrast to distinguish several molecular constituents of living organisms, delivering maps with high chemical specificity and high spatial resolution.³ On the downside, SR suffers from very low scattering cross sections due to its spontaneous nature, resulting in a long pixel dwell time of ≈ 1 s, which leads to acquisition times of up to several hours for a high spatial resolution image.⁴ These hurdles can be overcome employing coherent Raman scattering,^{5–9} in either the coherent anti-Stokes Raman scattering (CARS)¹⁰ or the stimulated Raman scattering (SRS)¹¹ modality. In particular, SRS is becoming the technique of choice since, differently from CARS, it shows a linear dependence on the concentration of resonant molecules¹² and is nearly immune from nonlinear effects unrelated to any vibrational transition, such as the so-called non-resonant background, that can distort or even overwhelm the vibrational response of the molecules under study.^{13,14}

SRS is a third-order nonlinear optical process originating from the spatiotemporal superposition of two light fields, the pump (at frequency ω_{pu}) and the Stokes (at frequency ω_S). At the sample plane, this superposition generates a beating at the pump-Stokes frequency detuning $\Omega = \omega_{pu} - \omega_S$. When Ω matches a vibrational mode Ω_R of a molecule, the resonance induces a coherent energy transfer between the driving fields and the molecule. This process enhances the nonlinear signal generation efficiency by many orders of magnitude with respect to SR,¹⁵ enabling chemically specific label-free imaging at high acquisition rates.^{16,17} Because of this nonlinear light-matter interaction, the molecule reaches a vibrationally excited state, and simultaneously, the Stokes pulse is amplified (a process known as stimulated Raman gain, SRG), while the pump pulse is attenuated (a process known as stimulated Raman loss, SRL).¹⁵ SRG and SRL are small signals (ΔI) sitting on top of an intense and fluctuating optical field (I), with $\Delta I/I$ typically ranging from 10^{-4} to 10^{-6} . To extract such tiny signals, one beam is modulated at high frequency (>1 MHz, where the laser noise reaches its minimum values), and the modulation transfer on the other beam is detected using a lock-in amplifier,¹¹ a resonant circuit,¹⁸ or a boxcar integrator.¹⁹ Thus, the laser noise is strongly suppressed and the imaging speed can be increased for a given target signal-to-noise ratio (SNR).²⁰

Conventional SRS microscopy employs narrowband (≈ 10 – 20 cm^{-1}) pump and Stokes pulses to image a sample at a single vibrational frequency, allowing imaging at speeds up to the video rate, with pixel dwell times as low as ≈ 100 ns.²¹ Notably, narrowband SRS microscopy working at two vibrational frequencies resonant to the lipid-rich and protein-rich regions of cells has even reached the operating room, delivering near-real-time diagnosis of fresh, unprocessed thin human tissue slices, which reveals structural features similar to those observed with the conventional cancer diagnosis, i.e., histopathology examination by hematoxylin and eosin (H&E) staining.²²

However, narrowband SRS working at just one or two vibrational frequencies is often not sufficient to differentiate chemical species with overlapping Raman bands, especially within heterogeneous systems,²³ e.g., a tissue or a cell. To exploit the full potential of SRS, broadband SRS realizations have been proposed to measure a vibrational spectrum of the sample at each image pixel. Broadband SRS can be classified as follows:²⁴ (i) hyperspectral SRS, which combines narrowband pump and Stokes pulses, for single-frequency SRS, with fast frequency tuning to rapidly build an SRS spectrum using a serial approach;^{25–30} (ii) multiplex SRS, in which one of the Stokes/pump pulses is broadband and the SRG/SRL spectrum is recorded by a parallel approach in the frequency domain using a multichannel detector.

Early experimental demonstrations of multiplex SRS used a spectrograph to disperse the broadband pulse onto a CCD or CMOS camera that digitizes the spectrum.^{31–33} However, these detectors only operate at low (<20 kHz) repetition rates, a range in which the noise floor of the laser is high, thus preventing fast imaging. Another approach consists of replacing the CCD/CMOS digital camera with a photodiode array. Kobayashi and co-workers^{34,35} coupled the array with a multichannel lock-in amplifier (M-LIA), a system that worked at low modulation frequencies (≈ 1 kHz), limiting the sensitivity for SRS detection. Liao *et al.*³⁶ instead coupled the photodiode array to a tuned amplifier (TAMP) array, based on an RLC circuit tuned to the 2.1 MHz modulation frequency, and managed to measure SRS spectra containing 16 vibrational frequencies in only 32 μs . However, the electronic components in the TAMP set the modulation frequency of the experiment, a setting that cannot be changed without re-designing and re-assembling the circuitry of the electronic instrumentation and might drift after thermal fluctuations of the passive elements composing the TAMP. Recently, Suzuki *et al.*³⁷ used sub-harmonically synchronized, pulse pair-resolved, wavelength-switched Stokes laser pulses for four-color SRS acquisition, attaining pixel dwell times as low as 210 ns. Despite its impressive acquisition speed, the approach described in Ref. 37 relies on a linear decomposition of the hyperspectral SRS data, a fitting algorithm that requires reference or Raman spectra known prior to the imaging experiments.

Here, we present a multiplex SRS microscope that incorporates a novel home-built high-frequency M-LIA.^{38,39} This electronic system is based on a custom integrated circuit, specifically designed in CMOS technology for Raman spectroscopy applications that allowed us to integrate several lock-in amplifiers into a single chip. Thus, we could scale the number of detection channels up to 32 without increasing the dimensions of the detection system. Furthermore, the lock-in technique allows the tunability of both the modulation frequency and the bandwidth (or integration time) of the experiments. Consequently, an SRS apparatus equipped with lock-in detection can maximize the SNR by changing its modulation frequency.

Our SRS microscope can record modulation transfers as low as 10^{-6} , with an integration time of 44 μs , delivering, in a single shot, broadband SRS spectra covering a bandwidth of ≈ 250 cm^{-1} in the CH stretching region with high spectral resolution (≈ 15 cm^{-1}). We demonstrate its capabilities in imaging different biological systems, including HepaRG cells cultivated with different fatty acids (oleic and palmitic acids), which present minimal biochemical differences, and cancer tissue slices. Our results show the superior

chemical specificity of broadband SRS microscopy over its narrow-band counterpart and, importantly, demonstrate its potential for histopathology in revealing the spectral signatures of healthy and diseased tissues.

METHODS

Optical source for broadband SRS microscopy

The optical source for our broadband SRS microscope starts with an ytterbium-fiber laser (Coherent, Fidelity HP), delivering pulses at a central wavelength of 1040 nm with a duration of 140 fs and average powers up to 10 W at a repetition rate of 80 MHz. We employ a 4 W fraction of the fundamental beam to generate narrowband ($\approx 15 \text{ cm}^{-1}$ FWHM) Stokes pulses using a high-finesse Fabry–Perot etalon (SLS optics). An acousto-optic modulator (AOM, AA Opto-Electronic) modulates the intensity of these pulses at high frequency in the 1–10 MHz range. In this work, we present results with a modulation frequency of 1.6 MHz. To maximize the modulation contrast, we used the first diffraction order of the AOM. The remaining 6 W fraction of the fundamental beam is frequency doubled in a 1 mm-thick lithium triborate (LBO) crystal. The resulting second-harmonic radiation pumps a home-made optical parametric oscillator (OPO), delivering broadband pump pulses for multiplex SRS microscopy. An amplified piezoelectric actuator (APF710, Thorlabs) controls the cavity length, allowing fine tuning of the pump spectrum. With respect to the previously reported scheme,⁴⁰ here we employ a 3 mm-thick LBO crystal as a nonlinear medium to achieve higher average power (up to 100 mW) and limit the bandwidth to the region of interest (786–798 nm), which corresponds to a pump-Stokes frequency detuning in the range of 2916–3107 cm^{-1} (see Fig. S6 in the [supplementary material](#)). This allows us to cover the entire high-frequency CH-stretching Raman region. Outside the OPO cavity, a prism compressor introduces a negative chirp (group delay dispersion $\text{GDD} \approx -12\,800 \text{ fs}^2$) to the pump pulses to compensate for the positive chirp caused by the high numerical aperture (NA) objectives of the microscope. This allows the pump pulses to be close to transform-limited duration at the sample plane. Thus, all its spectral components reach the sample simultaneously and are temporally overlapped with the Stokes pulse, leading to an optimal signal generation efficiency. For imaging, we put at the sample plane 47.0 mW in the Stokes beam and 20 mW in the broadband pump beam. After attenuation by the linear scattering, reflections on mirrors, and dispersion through the grating, we obtained $\approx 100 \mu\text{W}$ per spectral component of the pump beam at the detectors plane.

Multichannel lock-in detection for broadband SRS microscopy

A sketch of the experimental setup is reported in [Fig. 1\(a\)](#). To reduce the effects induced by the laser noise and increase the imaging speed, we equipped our system with in-line balanced detection (IBD).⁴¹ IBD is based on the generation of two co-propagating replicas of the same laser pulse, called the signal and reference, which undergo the same attenuation/scattering upon propagation through samples presenting spatial variations of transmission. Thus, IBD guarantees automatic (passive) balancing of the powers of the signal and reference. A birefringent YVO_4 plate placed on the pump

beam before the microscope generates the two orthogonally polarized replicas, with a relative time delay of $\approx 4.9 \text{ ps}$. Since this delay is much larger than the pulse duration and the Stokes pulse is overlapped in time and polarization with only the signal pulse, the SRS signal will only occur on the signal pulse. The pump/reference and the Stokes beams are combined with a dichroic mirror and sent to a home-built upright microscope, in which they are focused on the sample with a water-immersion objective [Chromatic aberration-Free (CFI) Plan Apo IR 60XC WI, NA = 1.27, Nikon]. At the focal plane of the microscope, the sample is raster scanned with a piezo stage (P-517.3CL, Physik Instrumente). Upon propagation through the sample, a high-numerical aperture objective (CFI Apo Lambda S 60 \times Oil, NA = 1.4, Nikon) collects the transmitted light. Then, the Stokes beam is filtered out, while the pump beam propagates through a polarizing beam splitter (PBS) cube that separates the reference and the signal replicas. Finally, two independent steering mirrors guide the signal and reference to their corresponding photodetector arrays. An electronic subtraction of the voltages generated at the two detectors enables us to remove the common laser noise, thus reaching close to shot-noise-limited sensitivity.

To measure the spectra of the reference and the signal beams for broadband SRS with IBD, the two photodiodes are replaced by two photodiode arrays (model A5C-35 from OSI Optoelectronics), each containing 32 pixels of 1 mm width and 3.9 mm height. Before the PBS, the pump spectrum is dispersed using a high-throughput diffraction grating with 1850 grooves/mm in the Littrow configuration (model T-1850-800 s, LightSmyth Technologies) and imaged onto the detector plane using a lens with a focal length of 500 mm [L1 in [Fig. 1\(a\)](#)] such that the resulting dispersion of the reference/signal beams at the detector plane is $\sim 0.5 \text{ nm/mm}$, corresponding to $7.8 \text{ cm}^{-1}/\text{mm}$, i.e., $7.8 \text{ cm}^{-1}/\text{pixel}$. This linear dispersion is adequate to resolve the spectral features of the investigated samples, as Raman linewidths in the solid phase are typically broader than 10 cm^{-1} . To calibrate the frequency axis of the system, we employed the reported vibrational peaks of solvents measured by SR spectroscopy. Fitting the SRL peak of DMSO centered around 2919 cm^{-1} to a Lorentzian curve, we estimated the full-width at half-maximum spectral resolution of our system as $\approx 15 \text{ cm}^{-1}$ (see the [supplementary material](#)).

While SRS does not suffer from the non-resonant background as CARS, it may undergo spurious nonlinear effects that are overlapped with the pure resonant vibrational signal. The main processes that distort an SRS spectrum are nonlinear transient absorption and cross-phase modulation (XPM).^{42–44} Both effects alter the pump beam and contribute to the SRL signal. Transient absorption occurs through resonant electronic transitions, while XPM occurs via changes in the sample refractive index experienced by the pump beam due to third-order nonlinear interaction with the Stokes. XPM, in concert with the finite NA of the collection objective, clips the pump beam and leads to substantial spurious SRL. The tissue scattering, the grating, and the limited dimensions of each pixel in the detector array could further exacerbate the effects of XPM. Because our system operates with near-infrared excitation, it avoids resonant transitions of biomolecules and, hence, transient absorption. In addition, our microscope collects the pump beam with a microscope objective whose NA ($\text{NA}_{\text{col}} = 1.4$) is larger than that of the excitation objective ($\text{NA}_{\text{ex}} = 1.27$). We noticed that this combination removed

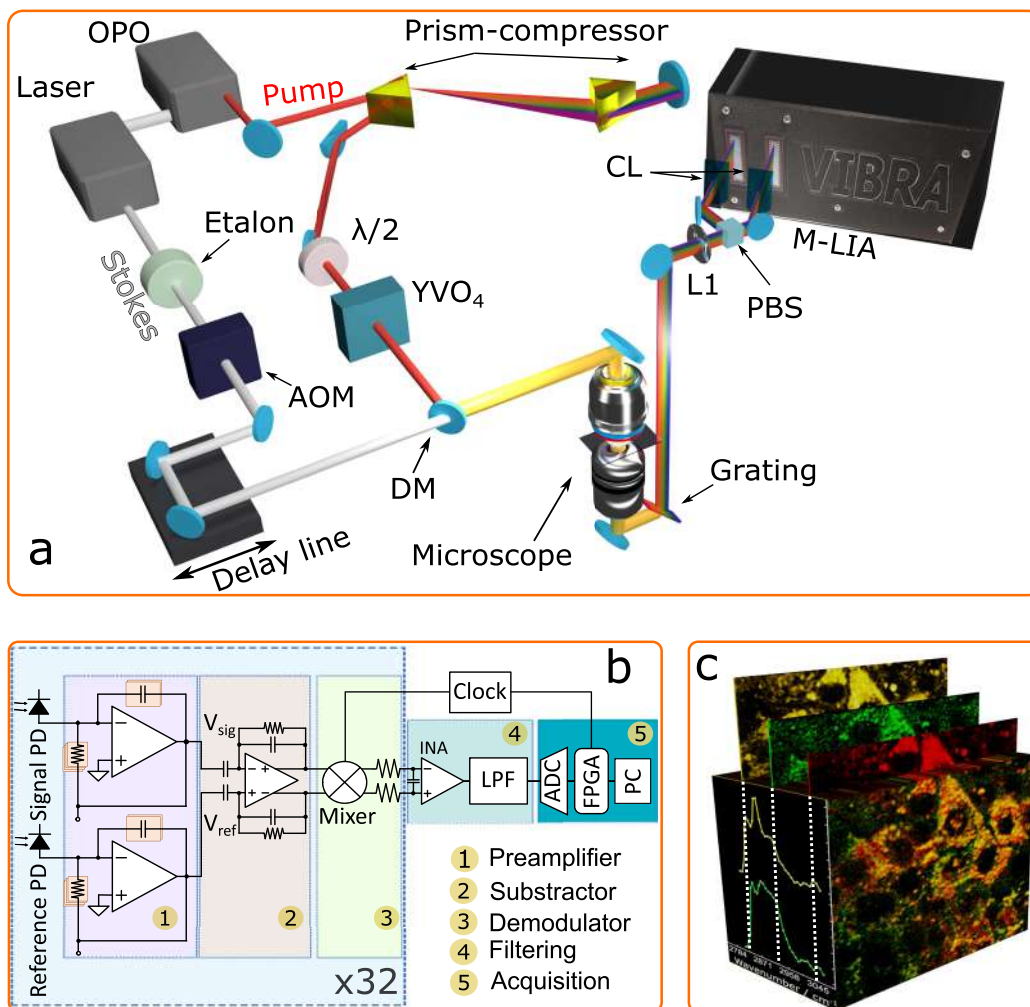


FIG. 1. Broadband SRS microscopy based on multi-channel lock-in detection: schematic representations of (a) the optical setup, (b) the electronic instrumentation composing a single channel, and (c) the data hypercube generated by SRS, which consists of an entire SRS spectrum per pixel, allowing one to form SRS maps at different vibrations. OPO: optical parametric oscillator, AOM: acousto-optic modulator, $\lambda/2$: half-wave plate, DM: dichroic mirror, PBS: polarizing beam splitter, M-LIA: multichannel-lock-in amplifier, CL: cylindrical lens, PD: photodiode, L1: spherical lens, INA: instrumentation amplifier, LPF: low-pass filter, ADC: analog to digital converter, and FPGA: field-programmable gate array.

any major contribution stemming from the XPM to the SRL signal. To further reduce the XPM effects, each pump replica, namely, the signal and reference, is focused on its corresponding detector array through a cylindrical lens. The axes of the cylindrical lenses are parallel to the detector array. This configuration redirects any slightly divergent spectral components of the pump along the long axis of each photodiode (which is orthogonal to the cylindrical lens axis), preventing spurious contributions to the SRL signal. Therefore, our system minimizes the spurious non-vibrational signals, guaranteeing authentic Raman spectra.

The electronic instrumentation of the broadband SRS microscope consists of a multi-channel differential readout system based on the lock-in technique. We have already introduced this board

previously for the simple case of four channels.³⁹ In this work, we extend this concept implementing balanced detection to simultaneously acquire the SRS spectrum over 32 different vibrational frequencies, effectively moving from *multi*-spectral to *hyper*-spectral SRS microscopy. Figure 1(b) illustrates a simplified scheme of the architecture of the system. Two silicon photodiode arrays measure the optical power of the spectral components of the signal and reference replicas. A pre-amplifier circuit [module 1 in Fig. 1(b)], coupled with the output of a photodiode, amplifies the current generated by the photodiode and separates the modulated signal (V_{ac}) from the voltage (V_{dc}) proportional to the average power incident on the photodiode. An amplifier array, presented in Fig. 1(b) with $H(s)$, carries out the splitting of the AC and DC components of the

photo-induced current at each photodiode (see details in Ref. 45). The digitized value of V_{dc} is stored, as it is necessary for the normalization of the SRS signal, i.e., $V_{ac}/V_{dc} \propto \Delta I/I$. Module 2 in Fig. 1(b) implements the analog subtraction of the signal and reference modulated signals V_{ac} to reduce, up to 32 dB, the common-mode laser noise of the pump beam. The noise characterization of the setup is presented in Fig. S5 in the supplementary material. A CMOS demodulator [module 3 in Fig. 1(b)] shifts V_{ac} from the modulation frequency of the Stokes beam to the baseband or DC.

Note that microcircuit integration of modules 1–3 allows us to scale the number of detection channels. An instrumentation amplifier converts the differential signal of the demodulator to a single-ended signal, which is subsequently low-pass filtered with a time constant of 10 μ s [see module 4 in Fig. 1(b)]. Finally, the filtered signal is digitized and normalized with V_{dc} and transferred to the computer (module 5). An FPGA (Xilinx, Artix-7) adjusts the demodulation clock for each channel, controls the raster scanning of the sample, synchronizes the SRS readings with their corresponding coordinate on the sample plane, and manages the serial communication with the computer.

Cell culture and treatment

Human hepatic HepaRG cells were seeded on transparent glass-bottomed dishes (Willco Wells) in proliferation medium [William's E medium with GlutaMAX (Gibco), supplemented with 10% FBS (Hyclone II GE), 1% penicillin/streptomycin (Sigma), 5 μ g/ml insulin (Sigma), and 0.5 μ M hydrocortisone hemisuccinate (Sigma)]. Cells were seeded at high density (1×10^5 cells/cm²) and left untreated or treated 24 h after seeding for 5 days with a combination of sodium oleate 250 μ M (Sigma) + sodium palmitate 100 μ M (Sigma), diluted in complete proliferation medium. Both sodium oleate and sodium palmitate stock solutions were prepared dissolving in 99% methanol at a concentration of 100 mM. After treatments, cells were fixed with 4% paraformaldehyde (diluted in 1 \times PBS) (Sigma).

Tissue preparation

Specimens used for SRS imaging were obtained from the transplanted MN/MCA1 cell fibrosarcoma mouse model.⁴⁶ Briefly, the MN/MCA1 cell line was cultured in RPMI-1640 medium supplemented with 10% fetal bovine serum, 1% L-glutamine, and 1% Pen/Strep. Before inoculation, cells were detached with Trypsin/EDTA and washed and diluted in saline solution. 50 μ l containing 10^5 MN/MCA1 cells was injected intramuscularly in the mouse hind leg. Three weeks after tumor cell injection, mice were sacrificed and tumor tissues were collected and fixed in 4% PFA overnight at 4 $^{\circ}$ C. Subsequently, tumor tissues were dehydrated by incubation in PBS + 40% sucrose solution overnight at 4 $^{\circ}$ C and finally embedded in an Optimal Cutting Temperature (OCT) compound.

6 μ m thickness frozen sections were cut with a cryostat, mounted inside two glass coverslips (24 \times 50 mm, 1.5, 170 μ m thickness; cat. Number D-38116, Menzel-Glaeser), and then sealed with an optimal cutting temperature compound and stored at -20° C prior to acquisition. After H&E staining, slides were scanned with a DotSlide BX virtual slide scanner (Olympus) equipped with an

apochromat 2 \times /N.A. 0.085 objective. OlyVIA image software (version 3.5, Olympus) was used to acquire in the entire section and to identify the regions of interest correspondent to the tumor–peritumoral interface areas.

Chemometrics of hyperspectral SRS data

We extracted concentration maps and spectral profiles from the SRS hyperspectral cubes using a chemometric method popularized by Taule and colleagues called multivariate curve resolution (MCR) analysis.^{47,48} For this approach, we assumed that our experimental data matrix \mathbf{D} , the unfolded SRL hypercube, is a linear combination of the concentration \mathbf{C} and the spectral profiles \mathbf{S} of the chemical constituents of the sample, i.e., $\mathbf{D} = \mathbf{C}\mathbf{S}^T + \mathbf{E}$. Here, \mathbf{E} is a matrix containing the experimental error, while the superscript T indicates the matrix transpose. As an initial step to separate \mathbf{C} and \mathbf{S} , we obtained the main components of a singular-value decomposition of our spectral data and used them as the initial guesses of the pure spectra \mathbf{S} . Having defined the initial estimates of the pure spectra, we could calculate $\mathbf{C} = \mathbf{D}\mathbf{S}(\mathbf{S}^T\mathbf{S})^{-1}$ and $\mathbf{S}^T = (\mathbf{C}^T\mathbf{C})^{-1}\mathbf{C}^T\mathbf{D}$. These new values of \mathbf{C} and \mathbf{S} were then optimized with an alternating least-squares (ALS) algorithm. Since SRS spectra do not change the sign, i.e., they do not turn negative, we constrained the alternating least-squares algorithm to deliver only positive results. The optimized \mathbf{C} and \mathbf{S} allowed us to construct a new matrix $\mathbf{D}^* = \mathbf{C}\mathbf{S}^T$, which was then contrasted against the original data \mathbf{D} . We iterated these steps until the difference between \mathbf{D}^* and \mathbf{D} was less than an arbitrary threshold value. Plots of \mathbf{C} and \mathbf{S} reveal the chemical images of the concentrations and spectral profiles of the chemical constituents of the sample, respectively.

Spontaneous Raman spectroscopy

Spontaneous Raman measurements were performed with a home-built confocal Raman microspectroscopy setup using a continuous-wave diode laser (Cobolt AB, Flamenco, Solna, Sweden) centered at 660 nm to drive the Raman signals. The pump beam was guided to a commercial microscope (IX73, Olympus Europa SE & Co. KG, Hamburg, Germany) with a single-edge dichroic beamsplitter (Di03-R660-t1-25x36, Semrock, Inc., Rochester, NY, USA). A dry/air 50 \times objective (MPLFLN50X 50 \times /0.80 NA, Olympus) focused the pump light on the samples, and in turn, it collected the backscattered Raman photons, guiding them back to the dichroic beamsplitter. A long-pass (664 nm) edge filter (LP02-664RU-25, Semrock, Inc.) removed the residual pump light, transmitting the Raman signal. Finally, a lens ($f = 35$ mm, AC254-035-B-ML, ThorLabs, Newton, NJ, USA) focused the Raman scattering on the entrance slit of a spectrometer (Isoplane 160, Teledyne Princeton Instruments, Trenton, NJ 08619 USA) equipped with a 1200 grooves/mm grating, which is coupled with a front illuminated CCD (Pixis 256, Teledyne Princeton Instruments, Trenton, NJ 08619 USA). The excitation power for all the spontaneous Raman experiments was kept at 50 mW. Each spontaneous Raman spectrum shown in Fig. 2 was obtained by averaging three spectral acquisitions with an integration time of 10 s; the spectra were pre-processed by subtracting the baseline (polynomial curve with degree 8). To calibrate the wavenumber axis, toluene and argon-mercury bands

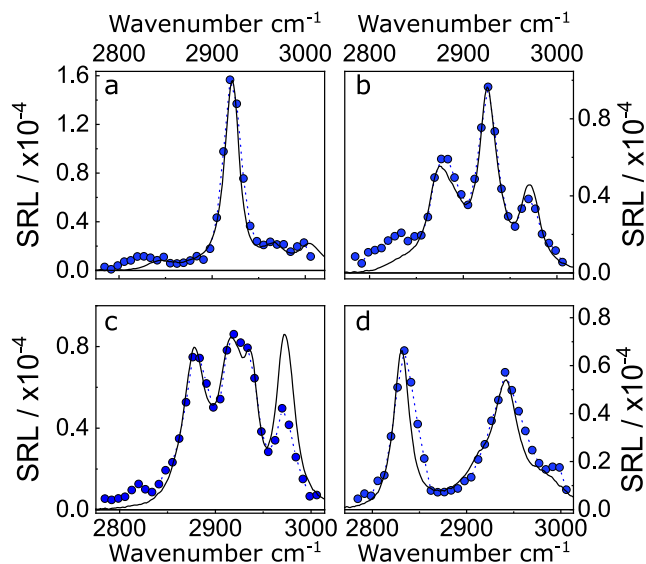


FIG. 2. Broadband SRS spectroscopy of solvents: stimulated Raman loss spectra of reference solvents: (a) acetone, (b) ethanol, (c) isopropanol, and (d) methanol acquired with an integration time of $44 \mu\text{s}$ for the entire spectrum. The black solid curves are the corresponding spontaneous Raman spectra.

(AvaLight-CAL (-Mini)—Avantes BV, Apeldoorn, The Netherlands) were used. The spectral intensity was corrected using a tungsten halogen light source with a known emission spectrum (Avalight-HAL; Avantes BV, Apeldoorn, The Netherlands).

RESULTS

Broadband SRS micro-spectroscopy

The experimental setup is shown in Fig. 1(a) and presented in detail in the Methods section. The optical source for our broadband SRS microscope starts with an ytterbium-fiber laser (Coherent, Fidelity HP), delivering pulses at a central wavelength of 1040 nm with a duration of 140 fs and average powers up to 10 W at a repetition rate of 80 MHz. We employ a 4 W fraction of the fundamental beam to generate narrowband (FWHM, $\approx 15 \text{ cm}^{-1}$) Stokes pulses using a high-finesse Fabry–Perot etalon (SLS optics). An acousto-optic modulator (AOM, AA Opto-Electronic) modulates the intensity of these pulses at a modulation frequency of 1.6 MHz. The other fraction of the laser pumps an OPO that delivers broadband fs-pulses. To further increase the SNR and approach the shot-noise limit, we use balanced detection^{49,50} (see Fig. 1 in the supplementary material). In particular, we employ a variant of balanced detection, namely, in-line balanced detection (IBD; Fig. 2 in the supplementary material),⁴¹ in which both the signal and reference beams propagate collinearly through the sample with perpendicular polarizations and the reference pulse is suitably anticipated in time with respect to the probe so that it does not undergo SRL. Since the two beams follow the same optical path, they experience equal attenuation due to the local absorption and scattering of the sample, thus providing an all-optical auto-balancing when raster-scanning the specimen. After the

sample, the narrowband Stokes pulse is filtered out, while the signal/reference pulse replicas are imaged using two cylindrical lenses on two 32-channel photodiode arrays whose outputs are sent to the signal and reference inputs of the M-LIA. The conceptual working principle of the M-LIA is sketched in Fig. 1(b) and described in detail in the Methods section and in Ref. 39.

Our broadband SRS microscope allows recording three-dimensional hyperspectral datacubes, datasets that consist of SRS spectra at 32 vibrational frequencies for each x–y position of a sample [see Fig. 1(c)]. These data offer true chemical contrast because they enable disentangling and spatially localizing different chemical species within heterogeneous specimens with overlapping vibrational spectra.

We first characterized the system performance by measuring the SRL spectra of different solvents, namely, acetone, ethanol, isopropanol, and methanol at an integration time of $44 \mu\text{s}$. As shown in Fig. 2, the SRL spectra of these reference solvents (data points) are in good agreement with their corresponding SR spectra (black solid line) and display a comparable frequency resolution. However, the spontaneous Raman spectra in Fig. 2 not only are in full agreement with tabulated Raman values but also have enough spectral resolution to reveal both the peaks and ratios of the Raman traces in the CH stretching, thereby providing authentic Raman spectra for validating our SRS system. We then tested the sensitivity of our system by measuring the SRL spectra of a set of DMSO/water solutions at various relative concentrations from 100% to 0%. We found that the system can detect the SRS spectra of DMSO at concentrations down to 1%, corresponding to 140 mM (see Fig. 3 in the supplementary material), at an M-LIA integration time of 1.3 ms.

Figure 3 shows the images, also acquired with an integration time of $44 \mu\text{s}$, of a sample constituted by $6 \mu\text{m}$ poly(methyl methacrylate) (PMMA) and $10 \mu\text{m}$ polystyrene (PS) microbeads placed between two coverslips and soaked in a mixture of olive oil and dimethyl sulfoxide (DMSO). All the imaging experiments were carried out with 47.0 mW in the Stokes beam and 20 mW in the pump beam ($\approx 100 \mu\text{W}$ per spectral component). Panels (a)–(d) show four of the 32 SRS images of the hyperspectral datacube at individual vibrational frequencies, chosen in correspondence to the most prominent peaks of the species of the sample [see gray bars in Fig. 3(f)]. We analyzed the data using the multivariate curve resolution-alternating least squares (MCR-ALS) algorithm,^{47,48,51,52} which decomposes the hyperspectral SRS datacube for the heterogeneous sample into a sum of spectra of the pure components [Fig. 3(f)] weighed by their concentration maps [Fig. 3(e)] (see the Methods section). The SRS spectra of the chemical constituents of the sample are in very good agreement with their SR counterparts, confirming the potential of hyperspectral SRS microscopy for the identification and localization of chemical species of a heterogeneous sample.

SRS mapping of fatty acids in hepatocytes

We next applied our imaging platform to map biochemical species within cultured cells. In particular, we investigated the uptake of saturated (palmitic) and unsaturated (oleic) fatty acids, which, depending on the diet, have been proved to influence cellular metabolism, toxicity, and morphology, playing an important role in metabolic diseases and cancer. Previous studies^{53–59} reported that,

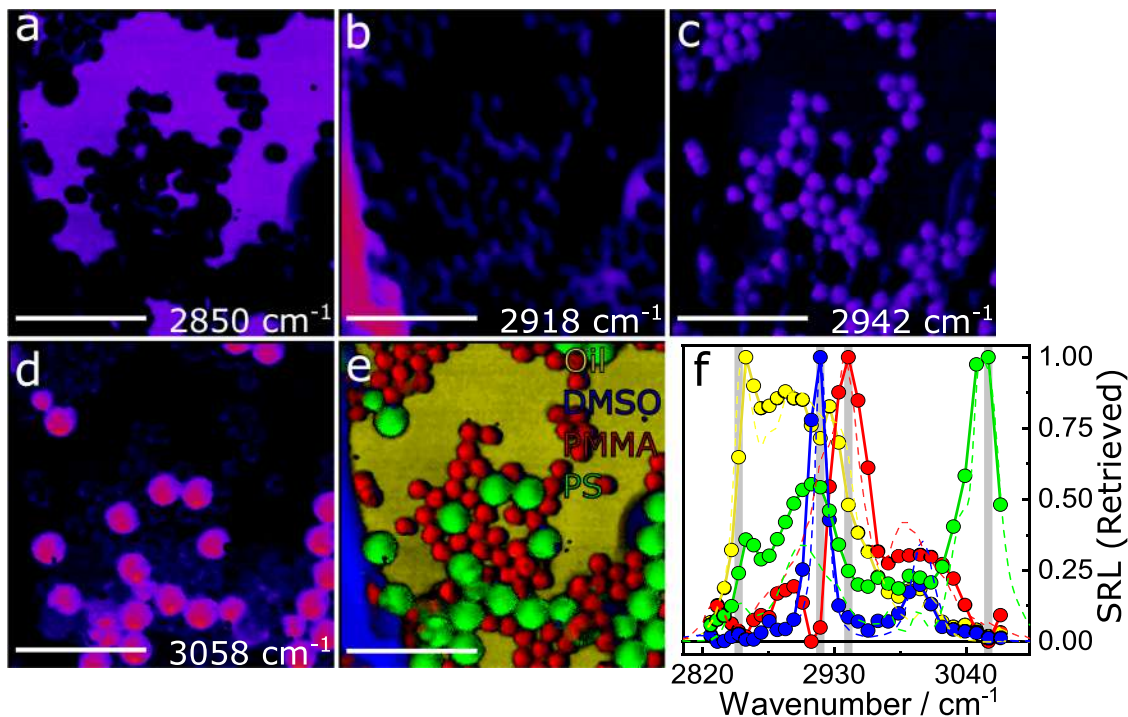


FIG. 3. Chemical imaging with broadband SRS microscopy. The broadband SRL imaging of a heterogeneous mixture of 10 μm PS and 6 μm PMMA beads immersed in olive oil and DMSO. Panels (a)–(d) show SRL images at the indicated Raman shift, corresponding to the peak of olive oil, DMSO, PMMA, and PS vibrational response [gray bars in (f)], respectively. (e) Concentration map of the four components and (f) corresponding SRL spectra, retrieved from the experimental data with MCR-ALS. The dashed lines in (f) correspond to spontaneous Raman spectra, traces that use the same color code as (e). The composite image of (e) uses the color code of (f). Imaging settings: 250 \times 250 pixels; M-LIA time constant, 44 μs ; and scale bar, 50 μm .

relative to cells dosed with saturated fatty acids, cells treated with unsaturated ones produce more and larger lipid droplets and exhibit more pronounced structural deformations. Given the strong chemical similarity of oleic acid (OA, $\text{C}_{18}\text{H}_{34}\text{O}_2$) and palmitic acid (PA, $\text{C}_{16}\text{H}_{32}\text{O}_2$), fast and label-free discrimination is a challenge. As an *in vitro* model system, we used HepaRG cell lines, well-established human bipotent progenitor cell lines, capable of differentiating as either early hepatic progenitor cells or completely mature human hepatocytes.⁵⁰ These cell lines serve as a model to assess drug metabolism and to study differentiation processes, carcinogenesis, and infections. We incubated HepaRG cells in a culture medium containing OA and PA fatty acids and imaged them with broadband SRS microscopy [Fig. 4(a)]. The images show chemical heterogeneity on the sub-micrometer scale, revealing several species with different vibrational resonances simultaneously occupying the interaction volume. This is clearly visible by looking at the red curves in Figs. 4(f) and 4(g), showing the SRS spectra at the yellow “x” and “+” marks of (a), respectively.

The overlap between the vibrational bands of OA and PA makes it difficult to evaluate their respective concentrations by narrowband SRS. To extract the chemical content of the images, we first obtained the pure SRS responses of OA and PA by convolving their SR spectra with the spectral instrumental response function (see the Methods section) of our SRS microscope. Then, we

considered a third component that includes the remaining chemical species (dominated by the contribution of the water buffer) derived by averaging the SRS spectra of regions outside the cells. These three spectral components are shown in Fig. 4(e). Finally, we fitted the SRS spectrum of each pixel of the datacube with a linear superposition of these three fixed spectral components using a variable concentration coefficient for each of them. As an example, the dotted curves in Figs. 4(f) and 4(g) depict the results of this fit for the pixels labeled as “x” and “+” in (a). From the weights of the component spectra, it is evident that OA [yellow curve in Fig. 4(e)] is the main component in Pixel x, whereas PA [green curve, Fig. 4(e)] dominates the contribution in Pixel +. The weights of the oleic and palmitic components on each pixel of the image allowed us to construct concentration maps of those chemical species [see Figs. 4(b) and 4(c)]. These images indicate that oleic droplets are larger than the palmitic droplets. Figure 4(d) shows a map of the difference between the normalized intensity of the oleic and palmitic concentration maps. Note that when the absolute contribution of OA (PA) to a specific pixel is larger than that of PA (OA), the color of that pixel tends toward red (blue). On the other hand, a pixel is colored in white if the absolute contribution of PA and OA is the same. From Fig. 4(d), we can see that most of this figure is colored in yellow, meaning that the concentration of OA dominates over that of PA.

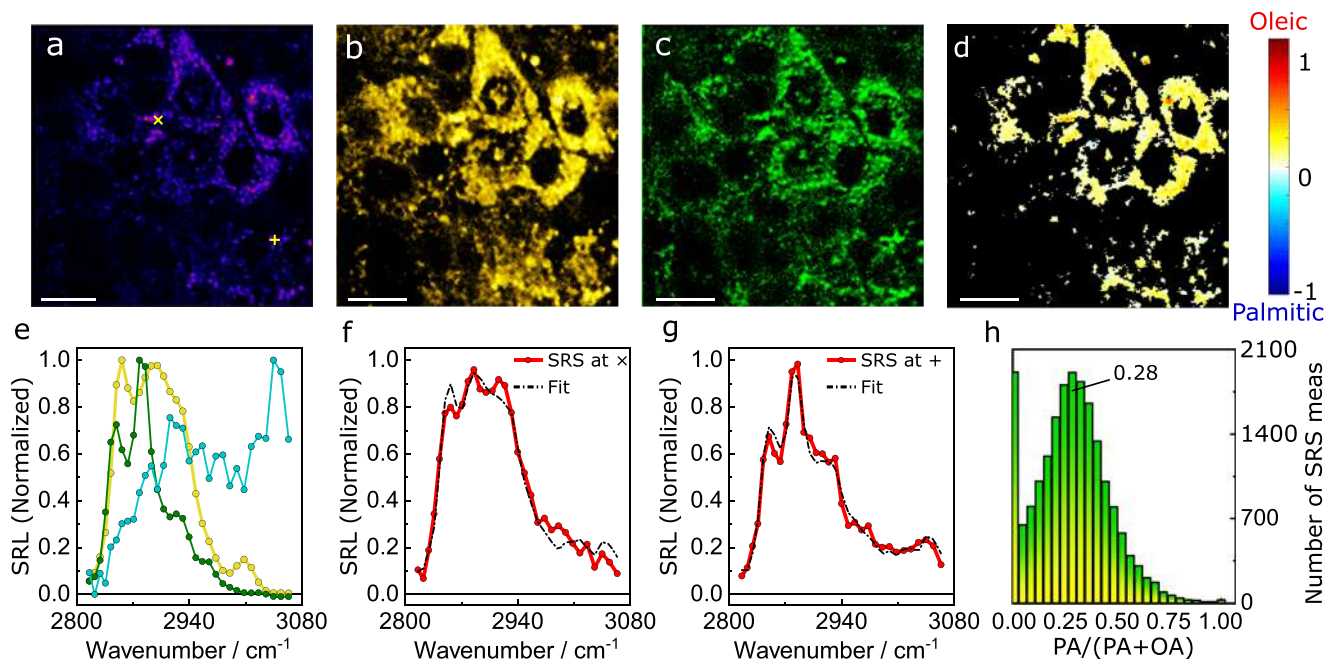


FIG. 4. Mapping fatty acid uptake in hepatocytes by broadband SRS: broadband SRS imaging of HepaRG cells grown in a culture media containing OA and PA fatty acids. (a) Typical SRL image of the cells at a single vibrational frequency (2845 cm^{-1}). (b) and (c) Concentration maps of OA and PA, respectively. (d) Difference between the normalized concentration maps of OA and PA. For better visualization, we excluded from the analysis those pixels with a weak SRS signal (sum of the spectral intensities of OA and PA below an arbitrary threshold value), colored in black in (d). (e) Spectral components used for the linear superposition: buffer (blue), OA (yellow), and PA (green). (f) and (g) Spectral information of the pixels labeled as \times and $+$ in (a), respectively: measured SRS spectra (red) and linear combination (black dotted curves) of the spectral components shown in (e). OA, PA, and buffer contributed 82%, 13%, and 5%, respectively, in the fit shown in (f), while for the fit in (g), they contributed 21%, 63%, and 16%, respectively. (h) Histogram depicting the fractional concentration of PA within the PA–OA mixture in the cells: $\text{PA}/(\text{PA} + \text{OA})$. Imaging settings: 286×286 pixels; M-LIA time constant, 1.2 ms; and scale bar, $20\ \mu\text{m}$.

The intensity maps of OA and PA shown in Figs. 4(b) and 4(c), respectively, also help to quantify the fractional uptake of triglycerides. Figure 4(h) depicts a histogram that represents the (relative) concentration of PA within the PA–OA mixture in the cells, i.e., $\text{PA}/(\text{PA} + \text{OA})$. Note that the last bin, which corresponds to 100% PA, is close to zero, signifying that HepaRG cells tend not to uptake PA only. In striking contrast, the first bin, which represents 100% OA, is among the most populated, indicating that the cells avidly absorb OA in the absence of PA. Since we provided the HepaRG cells $2.5\times$ excess of OA with respect to PA (see the Methods section), the dominant fractional concentration in Fig. 4(h) should be $1/(1 + 2.5) \approx 0.28$. Critically, the histogram shows a broad distribution centered around this value, revealing that the co-presence of OA facilitates the uptake of PA. Therefore, the histogram in Fig. 4(h) demonstrates the potential of our broadband SRS approach to not only distinguish and quantify different chemical species within heterogeneous biological samples but also elucidate biochemical mechanisms at play in cells.

These findings go beyond previous observations based on conventional imaging techniques, such as confocal fluorescence microscopy, that rely on the emission of lipophobic dyes to determine the lipid droplet accumulation in cells.^{57,61} Our results not only re-emphasize the potential of coherent Raman imaging techniques to study lipid droplets⁵⁶ but also demonstrate the capability of

broadband SRS microscopy to target and localize different fatty acids intracellularly, especially when chemical differences are minimal, quantifying the PA–OA interplay ruling the lipid uptake.

Broadband SRS microscopy for spectral histopathology

SRS microscopy allows mapping important biochemical constituents of tissue, resulting in chemical images that can enhance the accuracy of disease diagnoses.^{62,63} This chemical specificity, alongside the fast imaging rates of SRS microscopy, holds promise to deliver prompt and accurate histopathologic diagnoses even in the operating room.^{22,64} So far, such studies have employed narrowband SRS microscopy, targeting the CH_2 and CH_3 stretching modes at 2845 and 2930 cm^{-1} ,⁶⁵ respectively. The contrast produced by the CH_2 vibration reveals lipids, typically scattered within the cytoplasm of the cells and in the extracellular matrix. The CH_3 signal shows similar cytoplasmic features as CH_2 , but it contains an additional contribution from proteins so that the difference between the CH_3 and CH_2 images highlights the protein-rich cell nuclei. Dual-frequency SRS microscopy thus enables “virtual histopathology” by providing, in a completely label-free manner, images that are in good agreement with standard H&E stained tissue sections.⁶⁶ This approach has been applied to brain cancer,

a malignancy that shows rapid tumor cell proliferation within a lipid-rich environment, facilitating the detection of CH_2/CH_3 ^{22,63,64} signatures.

Broadband SRS microscopy has the potential to improve diagnostic accuracy by performing *spectral* histopathology, i.e., extracting information on the chemical composition of the sample over a broad vibrational spectrum, which goes beyond the morphological information provided by H&E or virtual histopathology that assesses the lipid and protein concentrations by measuring SRS images at just two vibrational frequencies.^{22,63,64} To demonstrate

the applicability of our SRS system for this purpose, we used an *in vivo* transplantable mouse model of fibrosarcoma. MN/MCA1 fibrosarcoma cells were intramuscularly injected into WT mice [see Fig. 5(a)]. Three weeks after tumor cell injection, tumor tissues were collected and prepared as described in the Methods section. We specifically analyzed the interfaces between tumoral and peritumoral regions [see Figs. 5(b) and 5(c)]. Multiplex SRS hyperspectral datacubes of unstained frozen tissue sections, acquired at 32 parallel channels, were compared with the H&E image of the adjacent, sequential tissue slice [Fig. 5(d)]. Both contrasts revealed differences

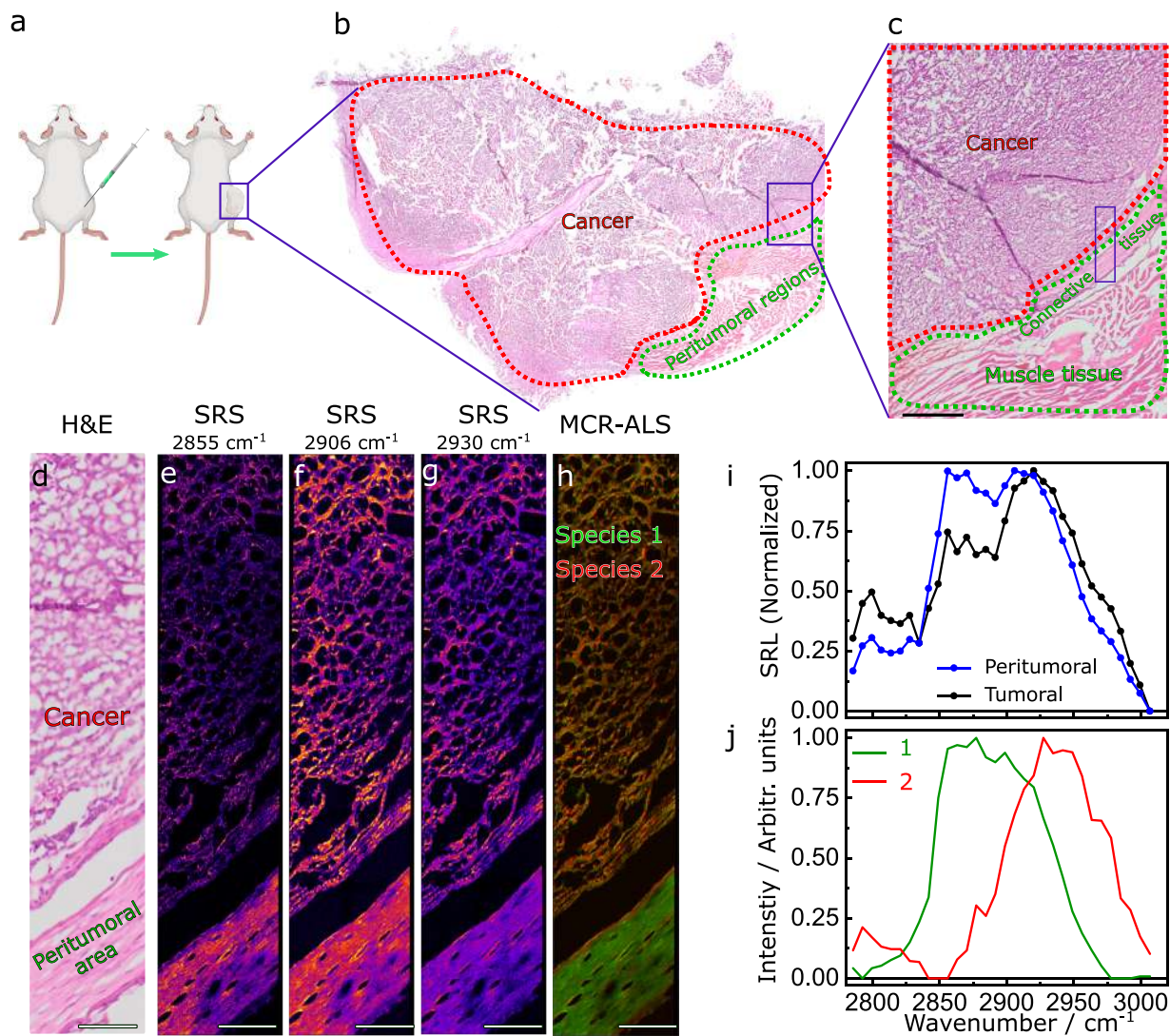


FIG. 5. Identification of mouse fibrosarcoma embedded in healthy tissue. (a) Cancer cells were injected into a mouse model to induce fibrosarcoma. (b) Bright-field image of a tissue slice labeled with H&E. (c) A zoom-in into an interface between tumor and peritumoral regions. In (c) and (d), the dotted-red and dotted-green lines enclose the cancerous and peritumoral regions, respectively. (d) Tissue portion investigated and discussed in the text. (e)–(g) SRS images at three different frequencies of a pristine sample corresponding to a sequential slide of the sample shown in (b)–(d). (h) Concentration maps of the SRS hypercube obtained by the MCR-ALS chemometric analysis. (i) Mean SRS spectra of peritumoral (blue) and tumoral (black) tissue. (j) Pure spectra obtained by MCR-ALS. In both (h) and (j), species 1 and 2 are colored in green and red, respectively. The scale bar in (c) is 1000 μm , while the scale bar in (d)–(h) is 100 μm . Imaging settings for (e)–(h): 2288 \times 572 pixels and M-LIA time constant, 1.2 ms.

between the peritumoral regions, delimited by connective tissue, and the spindle-shaped cells characteristic of fibrosarcoma⁶⁷ in the tumor area. Note that, even though the H&E and SRS images do not originate from the same tissue slice, there is not a substantial structural mismatch between the two contrasts that could hinder our comparison.

Figures 5(e)–5(g) show exemplary SRS images extracted from the datacube at three selected vibrational frequencies. Since each pixel of our images contains an entire vibrational spectrum, we could distinguish neoplastic and peritumoral tissue based not on morphological but on chemical information provided by the SRS spectrum. Figure 5(i) shows in blue the average of the SRS spectra from all the pixels within the healthy part of the tissue and in black the corresponding average spectrum from the diseased portion. Note that the spectra from both regions display a peak around 2930 cm^{-1} . However, the spectrum of the peritumoral tissue has a more pronounced peak around 2850 cm^{-1} .

To extract molecular concentration maps and spectral profiles from the SRS hyperspectral cubes, we employed both K-means analysis^{68,69} (see Fig. 4 in the [supplementary material](#)) and MCR-ALS. For the latter approach, we used the first three components of singular value decomposition as an initial guess for the concentrations *C* and the spectral profiles *S*. These three components accounted for the characteristic spectra observed in the peritumoral and tumoral tissue and the experimental noise. After convergence of the algorithm, the obtained concentration maps and the pure spectral components of the resolved species are shown in Figs. 5(h) and 5(j), respectively. Note that species 1 (colored in green) is distributed over the connective tissue, showing a spectrum evocative of the SR spectrum of lipidic species in the CH region. Species 2 (colored in red), however, is diffused across the cancerous region and manifests an associated spectrum reminiscent of the SR spectrum of proteins.^{65,66}

The spectra and concentration maps extracted with MCR-ALS suggest that the tumor contains a high concentration of proteins and few lipidic species. This finding is consistent with the nature of malignant tumors containing cells whose biochemical and structural characteristics differ from those detectable in peritumoral cells. Tumorous cells are characterized by a high proliferation rate and exhibit an abnormal nucleus–cytoplasm ratio. Consequently, tumorous cells within the same lesion vary in size and show an increased nuclear content, clustering into a tumor that is chemically homogeneous and rich in proteins. Furthermore, to infiltrate into healthy connective tissue, the fibroblasts employ an abnormally protein-rich extracellular matrix.^{67,70} Thus, the tumor lesion has an excess of proteins that contributes to the CH_3 contrast. MCR-ALS analysis also implies that the peritumoral tissue is packed with lipids and exhibits lower proteinic features. Compared to the tumor, the surrounding connective tissue is chemically more heterogeneous, as it contains an abundance of collagen and different cell types scaffolded within the extracellular matrix. Although these components are not lipid-rich structures, their joint CH_2 content leads to a higher lipidic contribution relative to that observed in the fibrosarcoma. Our observations are also in line with previous reports employing narrowband SRS microscopy that, through the ratio between the CH_3 (protein) and CH_2 (lipid) contrasts, inferred a higher concentration of proteins in tumorous tissue compared to peritumoral areas.⁶³ However, the broadband nature of our approach not only

allows rigorous spectral analysis but also increases the chemical specificity of SRS microscopy.

DISCUSSION

In this article, we presented a novel broadband SRS microscope featuring a differential multi-channel lock-in detection. We challenged the chemical specificity of our system by mapping hepatocytes dosed with an excess of fatty acids whose chemical structures are subtly distinct. In particular, we cultured HepaRG cells within a mixture of oleic and palmitic acids and mapped their distribution within the cells. We found that both lipidic species are absorbed by the cells. However, cells uptake more easily oleic acid than palmitic acid. While this is qualitatively in line with previous research on fatty acid homeostasis, here we quantify the relative contributions to a single droplet.

We demonstrated that our technology also enables spectral histopathology, delivering results consistent with the conventional H&E histological analysis. In fact, the chemical specificity and sensitivity of broadband SRS microscopy, assisted by chemometric analysis, allowed us to identify the main biochemical species within the analyzed regions, providing a solid biochemical ground for the discrimination of healthy regions from cancerous lesions of tissue sections of mouse fibrosarcoma. Specifically, we observed that the tumor contains a high concentration of proteins and few lipidic species, a consequence of the increased nuclear content of the fibroblasts, cells agglomerated into a neoplasm chemically homogeneous and rich in proteins. We also noticed that the healthy connective tissue is packed with lipids and exhibits lower proteinic features because, relative to the tumor, it is more chemically heterogeneous, which contains a wealth of collagen and different cell types scaffolded within a healthy extracellular matrix. The collective CH_2 content of the constituents of the healthy tissue leads to a higher lipidic contribution relative to that observed in the fibrosarcoma.

Future work will use this approach to investigate cellular dynamics *in vivo* and follow pathological processes *ex vivo* in both the fingerprint and CH stretch regions with an increased (up to 128) number of detection channels thanks to the scalability of the M-LIA architecture. Since our technology efficiently rejects laser noise, it is well suited for compact, turn-key fiber lasers^{49,71} that, although noisy, can generate broadband pulses, granting access to several molecular vibrations of cells and tissues simultaneously. Quieter laser sources, however, would lead to shorter integration times, down to hundreds of ns, thus enabling broadband SRS microscopy at video rates.

CONCLUSION

We have introduced a multiplex SRS microscope, incorporating a broadband optical source, a compact 32-channel integrated high-frequency lock-in amplifier, and in-line balanced detection to suppress laser noise. This microscope is able to acquire SRS spectra over the entire CH stretching region with high spectral resolution ($\approx 15\text{ cm}^{-1}$) and high acquisition rates (44–1300 μs integration time), combining the detailed spectral information of SR spectroscopy with the high acquisition speed of SRS. We have demonstrated the potential of our approach for chemical imaging of biological samples in

a label-free and non-invasive fashion, and we foresee that the compactness of our detection chain paves the way for the integration of broadband SRS into the clinics, introducing a technology that will complement and enhance the traditional histopathology workflow for tissue diagnosis.

SUPPLEMENTARY MATERIAL

See the [supplementary material](#) for a description of balanced detection and its variant in-line balanced detection, the spectroscopic characterization of the system, the K-means analysis of broadband SRS data of fresh tissue samples, the assessment of the noise canceling capabilities of the system, and a brief description of the optical source of the setup.

ACKNOWLEDGMENTS

D.P. acknowledges funding from the European Union project CRIMSON under Grant Agreement No. 101016923 and from the Regione Lombardia project NEWMED under Grant Agreement No. POR FESR 2014–2020. G.C. and T.S. acknowledge funding from the European Union project GRAPHENE Core3 under Grant Agreement No. 881603. G.C. and C.L. acknowledge funding from the King Abdullah University of Science and Technology under Grant Award No. OSR-2016-CRG5-3017-01. A.D.C. acknowledges the invaluable support and insights from Zülal Karaca throughout this research.

AUTHOR DECLARATIONS

Conflict of Interest

G.C. and A.R. declare involvement with the company Cambridge Raman Imaging, which aims to commercialize the broadband SRS microscopy technology. The other authors declare no competing interest.

Ethics Approval

Procedures involving animal handling and care were conformed to protocols approved by the Humanitas Research Hospital in compliance with national (D.L. N.116, G.U., suppl. 40, 18-2-1992 and N.26, G.U. 4 March 2014) and international law and policies (EEC Council Directive 2010/63/EU, OJ L 276/33, 22-09-2010; National Institutes of Health Guide for the Care and Use of Laboratory Animals, US National Research Council, 2011).

Author Contributions

Alejandro De la Cadena: Data curation (equal); Writing – original draft (equal). **Federico Vernuccio:** Investigation (equal). **Andrea Ragni:** Investigation (equal). **Giuseppe Sciortino:** Investigation (equal); Methodology (equal); Project administration (equal). **Renzo Vanna:** Methodology (equal); Project administration (equal); Resources (equal). **Carino Ferrante:** Software (equal). **Natalia Pediconi:** Investigation (equal). **Carlo Valensise:** Data curation (equal); Formal analysis (equal). **Luca Genchi:** Investigation (equal); Methodology (equal); Resources (equal). **Sergey P. Laptinok:** Formal analysis (equal). **Andrea Doni:** Resources (equal). **Marco Erreni:** Data curation (equal). **Tullio Scopigno:**

Investigation (equal). **Carlo Liberale:** Methodology (equal); Supervision (equal). **Giorgio Ferrari:** Investigation (equal); Methodology (equal). **Marco Sampietro:** Investigation (equal). **Giulio Cerullo:** Methodology (equal); Software (equal); Supervision (equal); Validation (equal); Writing – original draft (equal); Writing – review & editing (equal). **Dario Polli:** Software (equal); Supervision (equal); Validation (equal); Writing – original draft (equal); Writing – review & editing (equal).

DATA AVAILABILITY

The data that support the findings of this study are available at Zenodo, see [10.5281/zenodo.6772109](https://doi.org/10.5281/zenodo.6772109).

REFERENCES

- 1 A. Smekal, *Naturwissenschaften* **11**, 873 (1923).
- 2 C. V. Raman and K. S. Krishnan, *Nature* **121**, 501 (1928).
- 3 S. Stewart, R. J. Priore, M. P. Nelson, and P. J. Treado, *Annu. Rev. Anal. Chem.* **5**, 337 (2012).
- 4 R. Vanna, A. De la Cadena, B. Talone, C. Manzoni, M. Marangoni, D. Polli, and G. Cerullo, *La Riv. Del Nuovo Cimento* **45**, 107 (2021).
- 5 G. Eckhardt, R. W. Hellwarth, F. J. McClung, S. E. Schwarz, D. Weiner, and E. J. Woodbury, *Phys. Rev. Lett.* **9**, 455 (1962).
- 6 R. W. Hellwarth, *Phys. Rev.* **130**, 1850 (1963).
- 7 P. D. Maker and R. W. Terhune, *Phys. Rev.* **137**, A801 (1965).
- 8 N. Bloembergen, *Am. J. Phys.* **35**, 989 (1967).
- 9 M. D. Levenson, C. Flytzanis, and N. Bloembergen, *Phys. Rev. B* **6**, 3962 (1972).
- 10 A. Zumbusch, G. R. Holtom, and X. S. Xie, *Phys. Rev. Lett.* **82**, 4142 (1999).
- 11 C. W. Freudiger, W. Min, B. G. Saar, S. Lu, G. R. Holtom, C. He, J. C. Tsai, J. X. Kang, and X. S. Xie, *Science* **322**, 1857 (2008).
- 12 J.-X. Cheng and X. S. Xie, *Coherent Raman Scattering Microscopy* (CRC Press, Boca Raton, 2012).
- 13 Y. Liu, Y. J. Lee, and M. T. Cicerone, *Opt. Lett.* **34**, 1363 (2009).
- 14 C. M. Valensise, A. Giuseppe, F. Vernuccio, A. De la Cadena, G. Cerullo, and D. Polli, *APL Photonics* **5**, 061305 (2020).
- 15 H. Rigneault and P. Berto, *APL Photonics* **3**, 091101 (2018).
- 16 W. Min, C. W. Freudiger, S. Lu, and X. S. Xie, *Annu. Rev. Phys. Chem.* **62**, 507 (2011).
- 17 F. Hu, L. Shi, and W. Min, *Nat. Methods* **16**, 830 (2019).
- 18 M. N. Slipchenko, R. A. Oglesbee, D. Zhang, W. Wu, and J.-X. Cheng, *J. Biophotonics* **5**, 801 (2012).
- 19 R. J. Blume, *Rev. Sci. Instrum.* **32**, 1016 (1961).
- 20 X. Audier, S. Heuke, P. Volz, I. Rimke, and H. Rigneault, *APL Photonics* **5**, 011101 (2020).
- 21 B. G. Saar, C. W. Freudiger, J. Reichman, C. M. Stanley, G. R. Holtom, and X. S. Xie, *Science* **330**, 1368 (2010).
- 22 T. C. Hollon, B. Pandian, A. R. Adapa, E. Urias, A. V. Save, S. S. S. Khalsa, D. G. Eichberg, R. S. D'Amico, Z. U. Farooq, S. Lewis, P. D. Petridis, T. Marie, A. H. Shah, H. J. L. Garton, C. O. Maher, J. A. Heth, E. L. McKean, S. E. Sullivan, S. L. Hervey-Jumper, P. G. Patil, B. G. Thompson, O. Sagher, G. M. McKhann, R. J. Komotar, M. E. Ivan, M. Snuderl, M. L. Otten, T. D. Johnson, M. B. Sisti, J. N. Bruce, K. M. Muraszko, J. Trautman, C. W. Freudiger, P. Canoll, H. Lee, S. Camelo-Piragua, and D. A. Orringer, *Nat. Med.* **26**, 52 (2020).
- 23 B. Schrader, *Infrared and Raman Spectroscopy: Methods and Applications* (John Wiley & Sons, Weinheim, 2008).
- 24 D. Polli, V. Kumar, C. M. Valensise, M. Marangoni, and G. Cerullo, *Laser Photonics Rev.* **12**, 1800020 (2018).
- 25 Y. Ozeki, F. Dake, S. i. Kajiyama, K. Fukui, and K. Itoh, *Opt. Express* **17**, 3651 (2009).
- 26 L. Kong, M. Ji, G. R. Holtom, D. Fu, C. W. Freudiger, and X. S. Xie, *Opt. Lett.* **38**, 145 (2013).

- ²⁷J. Shou and Y. Ozeki, *Appl. Phys. Lett.* **113**, 033701 (2018).
- ²⁸S. P. Laptinok, V. P. Rajamanickam, L. Genchi, T. Monfort, Y. Lee, I. I. Patel, A. Bertoncini, and C. Liberale, *J. Biophotonics* **12**, 1 (2019).
- ²⁹A. De la Cadena, C. M. Valensise, M. Marangoni, G. Cerullo, and D. Polli, *J. Raman Spectrosc.* **5816**, 1951 (2020).
- ³⁰R. He, Z. Liu, Y. Xu, W. Huang, H. Ma, and M. Ji, *Opt. Lett.* **42**, 659 (2017).
- ³¹W. Rock, M. Bonn, and S. H. Parekh, *Opt. Express* **21**, 15113 (2013).
- ³²L. Czerwinski, J. Nixdorf, G. D. Florio, and P. Gilch, *Opt. Lett.* **41**, 3021 (2016).
- ³³F. E. Robles, K. C. Zhou, M. C. Fischer, and W. S. Warren, *Optica* **4**, 243 (2017).
- ³⁴K. Seto, Y. Okuda, E. Tokunaga, and T. Kobayashi, *Rev. Sci. Instrum.* **84**, 083705 (2013).
- ³⁵K. Seto, Y. Okuda, E. Tokunaga, and T. Kobayashi, *J. Phys. D: Appl. Phys.* **47**, 345401 (2014).
- ³⁶C.-S. Liao, M. N. Slipchenko, P. Wang, J. Li, S.-Y. Lee, R. A. Oglesbee, and J.-X. Cheng, *Light Sci. Appl.* **4**, e265 (2015).
- ³⁷Y. Suzuki, K. Kobayashi, Y. Wakisaka, D. Deng, S. Tanaka, C.-J. Huang, C. Lei, C.-W. Sun, H. Liu, Y. Fujiwaki, S. Lee, A. Isozaki, Y. Kasai, T. Hayakawa, S. Sakuma, F. Arai, K. Koizumi, H. Tezuka, M. Inaba, K. Hiraki, T. Ito, M. Hase, S. Matsusaka, K. Shiba, K. Suga, M. Nishikawa, M. Jona, Y. Yatomi, Y. Yalikul, Y. Tanaka, T. Sugimura, N. Nitta, K. Goda, and Y. Ozeki, *Proc. Natl. Acad. Sci. U. S. A.* **116**, 15842 (2019).
- ³⁸A. Ragni, G. Sciortino, M. Sampietro, G. Ferrari, and D. Polli, *Integration* **67**, 44 (2019).
- ³⁹G. Sciortino, A. Ragni, A. De la Cadena, M. Sampietro, G. Cerullo, D. Polli, and G. Ferrari, *IEEE J. Solid-State Circuits* **56**, 1859 (2021).
- ⁴⁰N. Coluccelli, D. Viola, V. Kumar, A. Perri, M. Marangoni, G. Cerullo, and D. Polli, *Opt. Lett.* **42**, 4545 (2017).
- ⁴¹F. Crisafi, V. Kumar, T. Scopigno, M. Marangoni, G. Cerullo, and D. Polli, *Sci. Rep.* **7**, 10745 (2017).
- ⁴²D. Fu, T. Ye, T. E. Matthews, G. Yurtsever, and W. S. Warren, *J. Biomed. Opt.* **12**, 054004 (2007).
- ⁴³P. Berto, E. R. Andresen, and H. Rigneault, *Phys. Rev. Lett.* **112**, 053905 (2014).
- ⁴⁴H. Zhu, H. J. Lee, and D. Zhang, *Stimulated Raman Scattering Microscopy* (Elsevier, 2022), pp. 137–146.
- ⁴⁵G. Ferrari and M. Sampietro, *Rev. Sci. Instrum.* **78**, 094703 (2007).
- ⁴⁶G. Germano, R. Frapolli, C. Belgiovine, A. Anselmo, S. Pesce, M. Liguori, E. Erba, S. Uboldi, M. Zucchetti, F. Pasqualini, M. Nebuloni, N. van Rooijen, R. Mortarini, L. Beltrame, S. Marchini, I. Fuso Nerini, R. Sanfilippo, P. G. Casali, S. Pilotti, C. M. Galmarini, A. Anichini, A. Mantovani, M. D'Incalci, and P. Allavena, *Cancer Cell* **23**, 249 (2013).
- ⁴⁷R. Tauler, *Chemom. Intell. Lab. Syst.* **30**, 133 (1995).
- ⁴⁸A. de Juan, J. Jaumot, and R. Tauler, *Anal. Methods* **6**, 4964 (2014).
- ⁴⁹A. Gambetta, V. Kumar, G. Grancini, D. Polli, R. Ramponi, G. Cerullo, and M. Marangoni, *Opt. Lett.* **35**, 226 (2010).
- ⁵⁰V. Kumar, M. Casella, E. Molotokaite, D. Gatti, P. Kukura, C. Manzoni, D. Polli, M. Marangoni, and G. Cerullo, *Phys. Rev. A* **86**, 053810 (2012).
- ⁵¹D. Zhang, P. Wang, M. N. Slipchenko, D. Ben-Amotz, A. M. Weiner, and J.-X. Cheng, *Anal. Chem.* **85**, 98 (2013).
- ⁵²I. Chitra Ragupathy, V. Schweikhard, and A. Zumbusch, *J. Raman Spectrosc.* **6184**, 1630–1642 (2021).
- ⁵³R. L. Hoover, K. Fujiwara, R. D. Klausner, D. K. Bhalla, R. Tucker, and M. J. Karnovsky, *Mol. Cell. Biol.* **1**, 939 (1981).
- ⁵⁴H. Malhi and G. Gores, *Semin. Liver Dis.* **28**, 360 (2008).
- ⁵⁵M. Ricchi, M. R. Odoardi, L. Carulli, C. Anzivino, S. Ballestri, A. Pinetti, L. I. Fantoni, F. Marra, M. Bertolotti, S. Banni, A. Lonardo, N. Carulli, and P. Loria, *J. Gastroenterol. Hepatol.* **24**, 830 (2009).
- ⁵⁶J. W. Schie, L. Nolte, T. L. Pedersen, Z. Smith, J. Wu, I. Yahiatène, J. W. Newman, and T. Huser, *Analyst* **138**, 6662 (2013).
- ⁵⁷B.-C. Cohen, A. Shamay, and N. Argov-Argaman, *PLoS One* **10**, e0121645 (2015).
- ⁵⁸J. Li, S. Condello, J. Thomes-Pepin, X. Ma, Y. Xia, T. D. Hurley, D. Matei, and J.-X. Cheng, *Cell Stem Cell* **20**, 303 (2017).
- ⁵⁹D. G. Abigail, T. Scopigno, N. Pediconi, M. Levrero, H. Hagman, J. Kiskis, and A. Enejder, “The histone deacetylase inhibiting drug Entinostat induces lipid accumulation in differentiated HepaRG cells,” *Sci. Rep.* **6**(1), (2016), <http://www.nature.com/articles/srep28025>.
- ⁶⁰M.-J. Marion, O. Hantz, and D. Durantel, in *Hepatocytes, Methods Molecular Biology*, 1st ed., edited by P. Maurel (Humana Press, 2010), pp. 261–272.
- ⁶¹H. Malhi, S. F. Bronk, N. W. Werneburg, and G. J. Gores, *J. Biol. Chem.* **281**, 12093 (2006).
- ⁶²C. W. Freudiger, R. Pfannl, D. A. Orringer, B. G. Saar, M. Ji, Q. Zeng, L. Ottonboni, W. Ying, C. Waerber, J. R. Sims, P. L. De Jager, O. Sagher, M. A. Philbert, X. Xu, S. Kesari, X. S. Xie, and G. S. Young, *Lab. Invest.* **92**, 1492 (2012).
- ⁶³M. Ji, D. A. Orringer, C. W. Freudiger, S. Ramkissoon, X. Liu, D. Lau, A. J. Golby, I. Norton, M. Hayashi, N. Y. R. Agar, G. S. Young, C. Spino, S. Santagata, S. Camelo-Piragua, K. L. Ligon, O. Sagher, and X. S. Xie, *Sci. Transl. Med.* **5**, 201ra119 (2013).
- ⁶⁴D. A. Orringer, B. Pandian, Y. S. Niknafs, T. C. Hollon, J. Boyle, S. Lewis, M. Garrard, S. L. Hervey-Jumper, H. J. L. Garton, C. O. Maher, J. A. Heth, O. Sagher, D. A. Wilkinson, M. Snuderl, S. Venneti, S. H. Ramkissoon, K. A. McFadden, A. Fisher-Hubbard, A. P. Lieberman, T. D. Johnson, X. S. Xie, J. K. Trautman, C. W. Freudiger, and S. Camelo-Piragua, *Nat. Biomed. Eng.* **1**, 0027 (2017).
- ⁶⁵F.-K. Lu, S. Basu, V. Igras, M. P. Hoang, M. Ji, D. Fu, G. R. Holtom, V. A. Neel, C. W. Freudiger, D. E. Fisher, and X. S. Xie, *Proc. Natl. Acad. Sci. U. S. A.* **112**, 11624 (2015).
- ⁶⁶B. Sarri, F. Poizat, S. Heuke, J. Wojak, F. Franchi, F. Caillol, M. Giovannini, and H. Rigneault, *Biomed. Opt. Express* **10**, 5378 (2019).
- ⁶⁷N. U. Din, K. Minhas, M. S. Shamim, N. Mushtaq, and Z. Fadool, *Child's Nerv. Syst.* **31**, 2145 (2015).
- ⁶⁸O. Ryabchikov, S. Guo, and T. Bocklitz, *Phys. Sci. Rev.* **4**, 20170043 (2019).
- ⁶⁹P. Wang, B. Liu, D. Zhang, M. Y. Belew, H. A. Tissenbaum, and J.-X. Cheng, *Angew. Chem.* **126**, 11981 (2014).
- ⁷⁰V. Poltavets, M. Kochetkova, S. M. Pitson, and M. S. Samuel, *Front. Oncol.* **8**, 431 (2018).
- ⁷¹C. W. Freudiger, W. Yang, G. R. Holtom, N. Peyghambarian, X. S. Xie, and K. Q. Kieu, *Nat. Photonics* **8**, 153 (2014).